Optimal rendezvous trajectory between Sample Return Orbiter and Orbiting Sample Container in a Mars Sample Return mission

Alberto Fossà, Carlo Bettanini

Optimal rendezvous trajectory between Sample Return Orbiter and Orbiting Sample Container in a Mars Sample Return mission

Alberto Fossà[a,b,*], Carlo Bettanini[b,c]

[a] ISAE Supaéro - Institut Supérieur de l'Aéronautique et de l'Espace, 10 Avenue Édouard Belin, Toulouse, France
[b] Department of Industrial Engineering, University of Padova, Via Venezia 1, Padova, Italy
[c] CISAS -Center for Studies and Activities for Space "G.Colombo", University of Padova, Via Venezia 15, Padova, Italy

Keywords:
Two-impulse rendezvous
Minimum energy
Non-coplanar elliptical orbits
Orbit transfer
Sample return

A B S T R A C T

A trajectory optimization problem is examined to determine the most fuel-efficient rendezvous trajectory between spacecrafts in different orbits. To explore the whole range of feasible solutions, the wait time and the total time of flight are treated as free parameters while the initial and transfer orbits are not restricted to a particular one. To improve the accuracy of the numerical computation, the Kepler's time of flight equation is posed in terms of universal variables while the Lagrange coefficients are employed to obtain three-dimensional orbit information. The optimal rendezvous trajectory is then obtained enforcing the determined necessary conditions to be satisfied given only the initial state vectors of the involved spacecrafts. Two optimal rendezvous trajectories between a Sample Return Orbiter (SRO) and an Orbiting Sample Container (OS) are computed in the context of a future Mars Sample Return mission to demonstrate the reliability of the proposed solution. Finally, orbital perturbations due to the real shape of planet Mars and the solar radiation pressure are taken into account to determine the additional energy required to compensate these perturbations while performing the rendezvous manoeuvre.

1. Introduction

1.1. Context

Mars exploration is a milestone in the Global Exploration Roadmap proposed by the International Space Exploration Coordination Group [1] as is a common interest in the future exploration activity by several international agencies. It provides global opportunities for scientific study and technological advancement and features at first robotic missions with the long-term goal of crewed landers on Mars [2] as a logical step for expanding human presence in the solar system. To enable sustainable human missions, a better understanding of environmental conditions and potential in-situ material utilization [3] shall be conducted by analysing samples from planetary surface.

Consequently, a Mars Sample Return mission [4–6] is perceived as a powerful way to answer most of the open questions about the red planet, enabling the international network of scientific laboratories and research facilities to conduct detailed analysis directly on the collected samples. The latest proposals for such a mission [5,7] subdivide the complex task into four different phases: samples collection from the surface of Mars and sealing in an Orbiting Sample Container (OS), launch of the OS in a parking orbit around the red planet, capture of the OS by a Sample Return Orbiter (SRO) and return of the SRO towards the Earth.

Due to multiple constraints on the SRO manoeuvring capabilities [8], the most fuel-efficient transfer trajectory to capture the passive OS has to be determined in order to increase the reliability of the whole mission. Assuming the first phase to be accomplished by the upcoming Mars 2020 rover, the OS will be placed in a low-inclined circular orbit while the SRO operating orbit will be most likely sun-synchronous for scientific purposes [4]. As a consequence, the most fuel-efficient transfer between two non-coplanar elliptical orbits has to be determined to satisfy the mission requirements.

1.2. Optimal control problem

The optimal control problem is then formulated assuming that the SRO will execute two impulsive manoeuvres to leave the initial parking orbit and perform the final rendezvous with the OS. Then, a specific approach is proposed to compute the optimal rendezvous trajectory between an active *chaser* and a passive *target* assuming that only the respective initial state vectors are known [9,10]. To explore the whole

* Corresponding author. ISAE Supaéro - Institut Supérieur de l'Aéronautique et de l'Espace, 10 Avenue Édouard Belin, Toulouse, France.
E-mail address: alberto.fossa18@gmail.com (A. Fossà).

https://doi.org/10.1016/j.actaastro.2020.02.046

range of feasible solutions, the wait time spent by the chaser in its initial orbit and the total time of flight required to complete the manoeuvre are left as free parameters to be determined. Finally, is to be noticed that the proposed approach is substantially different from most of the work presented in the literature, since the last relies frequently on the well known solution to the fixed-time Lambert problem.

In this work two meaningful *rendezvous conditions* are derived and it will be proven that the control energy required to perform the rendezvous is a minimum only if they are both satisfied [10]. These conditions are then adjoined with the required equations of motion to obtain a unique set of equations to be solved for the optimal transfer trajectory providing only the chaser and target's initial state vectors.

The proposed implementation is firstly validated on a test case proposed by Shirazi et al. [11] and then employed in the context of a future Mars Sample Return mission. For the last case, two optimal rendezvous trajectories that allow the SRO to capture the OS will be computed taking advantage of the developed optimization framework. For both cases, the numerical results and the required velocity changes are compared to the fixed-time solution to the Lambert problem to demonstrate the effectiveness of the proposed approach while searching for the most fuel-efficient transfer.

Since the whole optimization framework relies on the restricted two-body problem approximation, the last chapter relaxes this assumption to estimate the additional velocity changes to be undertaken by the SRO when the effects of the Mars static gravitational field and the solar radiation pressure are taken into account. A parametric study is conducted here to determine the impact in the overall Δv due to variations in each orbital parameter of both SRO and OS.

The paper is organized as follows. Before being applied in the subsequent work, the Kepler's equation in terms of universal variables and the Lagrange coefficients are briefly revised in chapter 2. Secondly, chapter 3 defines a cost index to evaluate the optimal solution and resumes the derivation of the two rendezvous conditions. The chapter concludes with the presentation of the whole set of equations to be solved for the optimal rendezvous trajectory. Thirdly, chapter 4 compares the test case results with the ones presented in the literature while in chapter 5 two possible solutions for the Mars Sample Return mission are computed and validated comparing the proposed approach with the solution to the Lambert problem. Finally, chapter 6 presents the consequences of the considered orbital perturbations on the SRO performances while chapter 7 draws some general conclusions on the conducted work.

2. Mathematical background

2.1. Kepler's equation

To simplify the spacecrafts' equations of motion and the derivation of the optimality conditions the first fundamental assumption is to consider the planet Mars to be a spherical and homogeneous body. Moreover, the gravitational forces due to other celestial bodies in the solar system and non-gravitational phenomena such as the solar radiation pressure are neglected. Under these hypothesis the subsequent work is formulated in the restricted two-body problem framework, for which the well-known Kepler's equation holds [12]:

$$M_e = E - e\sin E \tag{1}$$

With M_e mean motion, E eccentric anomaly and e eccentricity of the orbit. Here $M_e = \sqrt{\mu/a^3}\,(t - t_p)$ where t is the time at which the position is computed while t_p is referred to the periapsis passage.

However, equation (1) is valid only for elliptical orbits with $e < 1$ and its numerical solution for t when the spacecraft's position is known becomes inaccurate for almost parabolic orbits with $e \to 1$. To overcome this issue an alternative formulation based on the universal variables is introduced in section 2.2.

2.2. Universal variables

Starting from the classical orbital elements, the universal variable is defined as [13]:

$$\dot{x} = \frac{\sqrt{\mu}}{r} \tag{2}$$

where μ is the gravitational parameter of the central body and r the spacecraft's position.

Then, assuming $t_0 = 0$ for $x = 0$ and denoting with $[\boldsymbol{r}_0, \boldsymbol{v}_0]$ the state vector of the spacecraft at t_0 the two quantities r, t can be expressed as functions of x as given by equations (3) and (4):

$$\sqrt{\mu}\,t = a\left(x - \sqrt{a}\sin\frac{x}{\sqrt{a}}\right) + a\frac{\boldsymbol{r}_0^T\boldsymbol{v}_0}{\sqrt{\mu}}\left(1 - \cos\frac{x}{\sqrt{a}}\right) + r_0\sqrt{a}\sin\frac{x}{\sqrt{a}} \tag{3}$$

$$r = a + a\left[\frac{\boldsymbol{r}_0^T\boldsymbol{v}_0}{\sqrt{\mu a}}\sin\frac{x}{\sqrt{a}} + \left(\frac{r_0}{a} - 1\right)\cos\frac{x}{\sqrt{a}}\right] \tag{4}$$

2.3. Lagrange coefficients

Finally, since in the restricted two-body problem the spacecraft's motion is confined within a plane its state vector $[\boldsymbol{r}, \boldsymbol{v}]$ at time t can be expressed as a linear combination of $[\boldsymbol{r}_0, \boldsymbol{v}_0]$ at time t_0 as follows [12]:

$$\boldsymbol{r} = f\boldsymbol{r}_0 + g\boldsymbol{v}_0 \tag{5}$$

$$\boldsymbol{v} = \dot{f}\,\boldsymbol{r}_0 + \dot{g}\boldsymbol{v}_0 \tag{6}$$

Where $f, g, \dot{f}, \dot{g}$ are the four Lagrange coefficients whose expressions for an elliptical orbit are given by equations (7)–(10) [13]:

$$f = 1 - \frac{a}{r_0}\left(1 - \cos\frac{x}{\sqrt{a}}\right) \tag{7}$$

$$g = t - \frac{a}{\sqrt{\mu}}\left(x - \sqrt{a}\,\sin\frac{x}{\sqrt{a}}\right) \tag{8}$$

$$\dot{f} = -\frac{\sqrt{\mu a}}{r r_0}\sin\frac{x}{\sqrt{a}} \tag{9}$$

$$\dot{g} = 1 - \frac{a}{r}\left(1 - \cos\frac{x}{\sqrt{a}}\right) \tag{10}$$

Consequently, the three-dimensional motion of the spacecraft in a given orbit can be fully determined computing its state vector $[\boldsymbol{r}, \boldsymbol{v}]$ at any time t from the knowledge of $[\boldsymbol{r}_0, \boldsymbol{v}_0]$ at t_0 solving equations (3)–(10). This formulation is used in chapter 3 to derive the necessary conditions for an optimal rendezvous manoeuvre and in chapters 4–5 to obtain a numerical solution in the proposed scenarios.

3. Optimal control problem

3.1. Performance index

To solve for the most energy-efficient rendezvous trajectory a cost or *performance index* $\mathscr{J}$ is defined and the necessary conditions for its minimum derived analytically before proceeding with a numerical computation of the optimal solution.

Since the chaser performs the rendezvous manoeuvre with two consecutive impulsive burns, minimize the control energy is equivalent to minimize the instantaneous changes in the spacecraft's specific kinetic energy [14] and thus a convenient expression for $\mathscr{J}$ is given by:

$$\mathscr{J} = \frac{1}{2}\Delta\boldsymbol{v}_1^T\Delta\boldsymbol{v}_1 + \frac{1}{2}\Delta\boldsymbol{v}_2^T\Delta\boldsymbol{v}_2 \tag{11}$$

Where $\Delta\boldsymbol{v}_1$ is applied after the wait time t_1 to move the chaser from the

initial orbit to the transfer trajectory while $\Delta\boldsymbol{v}_2$ is applied after t to leave the transfer trajectory and enter the target orbit.

3.2. Constraints

A first constraint has to be added to the problem such that at each time the two spacecrafts follows a Keplerian orbit satisfying equations (3) and (4). This condition is easily expressed by equation (12) where $\boldsymbol{\eta} = [\eta_1, \eta_2, \eta_3]^T \in \mathscr{R}^3$ and the three components are given by equations (13)–(15).

$$\boldsymbol{\eta}(\bar{x}, x_1, x, t, t_1, \Delta\boldsymbol{v}_1) = 0 \tag{12}$$

$$\eta_1(\bar{x}, t) = \bar{a}\left(\bar{x} - \sqrt{\bar{a}}\sin\frac{\bar{x}}{\sqrt{\bar{a}}}\right) + \bar{a}\frac{\bar{\boldsymbol{r}}_0^T\bar{\boldsymbol{v}}_0}{\sqrt{\mu}}\left(1 - \cos\frac{\bar{x}}{\sqrt{\bar{a}}}\right) + \bar{r}_0\sqrt{\bar{a}}\sin\frac{\bar{x}}{\sqrt{\bar{a}}} - \sqrt{\mu}\,t \tag{13}$$

$$\eta_2(x_1, t_1) = a_0\left(x_1 - \sqrt{a_0}\sin\frac{x_1}{\sqrt{a_0}}\right) + a_0\frac{\boldsymbol{r}_0^T\boldsymbol{v}_0}{\sqrt{\mu}}\left(1 - \cos\frac{x_1}{\sqrt{a_0}}\right) + r_0\sqrt{a_0}\sin\frac{x_1}{\sqrt{a_0}} - \sqrt{\mu}\,t_1 \tag{14}$$

$$\eta_3(x_1, x, t, t_1, \Delta\boldsymbol{v}_1) = a_1\left(x - \sqrt{a_1}\sin\frac{x}{\sqrt{a_1}}\right) + a_1\frac{\boldsymbol{r}_1^T(\boldsymbol{v}_1 + \Delta\boldsymbol{v}_1)}{\sqrt{\mu}}\left(1 - \cos\frac{x}{\sqrt{a_1}}\right) + r_1\sqrt{a_1}\sin\frac{x}{\sqrt{a_1}} - \sqrt{\mu}\,(t - t_1) \tag{15}$$

Here 13 describes the motion of the target in an orbit with semi-major axis $\bar{a}$, while 14 and 15 represent the motion of the chaser in its initial orbit and in a transfer trajectory characterized by a_0 and a_1 respectively. Moreover, equation (13) holds in the time interval $[t_0, t]$, 14 in $[t_0, t_1]$ and 15 in $[t_1, t]$ where t_1 is the wait time and t the total time of flight.

Secondly, two more constraints are enforced to guarantee that at time t the two spacecrafts move along the same orbit and have the same positions as required by equations (16) and (17):

$$\bar{\boldsymbol{r}} - \boldsymbol{r} = 0 \tag{16}$$

$$\bar{\boldsymbol{v}} - (\boldsymbol{v} + \Delta\boldsymbol{v}_2) = 0 \tag{17}$$

Finally, the state vector $[\boldsymbol{r}_1, \boldsymbol{v}_1]$ of the chaser at t_1 and the two state vectors $[\boldsymbol{r}, \boldsymbol{v}]$ and $[\bar{\boldsymbol{r}}, \bar{\boldsymbol{v}}]$ for both spacecrafts at the final time t can be evaluated from equations (5) and (6):

$$\boldsymbol{r}_1(x_1, t_1) = f_0\boldsymbol{r}_0 + g_0\boldsymbol{v}_0 \tag{18}$$

$$\boldsymbol{v}_1(x_1) = \dot{f}_0\boldsymbol{r}_0 + \dot{g}_0\boldsymbol{v}_0 \tag{19}$$

$$\boldsymbol{r}(x_1, x, t, t_1, \Delta\boldsymbol{v}_1) = f_1\boldsymbol{r}_1 + g_1(\boldsymbol{v}_1 + \Delta\boldsymbol{v}_1) \tag{20}$$

$$\boldsymbol{v}(x_1, x, \Delta\boldsymbol{v}_1) = \dot{f}_1\boldsymbol{r}_1 + \dot{g}_1(\boldsymbol{v}_1 + \Delta\boldsymbol{v}_1) \tag{21}$$

$$\bar{\boldsymbol{r}}(\bar{x}, t) = \bar{f}\,\bar{\boldsymbol{r}}_0 + \bar{g}\bar{\boldsymbol{v}}_0 \tag{22}$$

$$\bar{\boldsymbol{v}}(\bar{x}) = \dot{\bar{f}}\,\bar{\boldsymbol{r}}_0 + \dot{\bar{g}}\bar{\boldsymbol{v}}_0 \tag{23}$$

While the semi-major axis of the transfer trajectory a_1 and the final orbit radius r can be computed from the energy equation and expression 4:

$$\frac{(\boldsymbol{v}_1 + \Delta\boldsymbol{v}_1)^T(\boldsymbol{v}_1 + \Delta\boldsymbol{v}_1)}{2} - \frac{\mu}{r_1} = -\frac{\mu}{2a_1} \tag{24}$$

$$r = a_1 + a_1\left[\frac{\boldsymbol{r}_1^T(\boldsymbol{v}_1 + \Delta\boldsymbol{v}_1)}{\sqrt{\mu a_1}}\sin\frac{x}{\sqrt{a_1}} + \left(\frac{r_1}{a_1} - 1\right)\cos\frac{x}{\sqrt{a_1}}\right] \tag{25}$$

3.3. Problem statement

Considering the performance index $\mathscr{J}$ defined in 11 and the constraints 12, 16 and 17, the optimal control problem is stated as follows: given $[\boldsymbol{r}_0, \boldsymbol{v}_0]$ and $[\bar{\boldsymbol{r}}_0, \bar{\boldsymbol{v}}_0]$ at time t_0 determine the wait time t_1, the total time of flight t and the velocity changes $\Delta\boldsymbol{v}_1$, $\Delta\boldsymbol{v}_2$ minimizing $\mathscr{J}$ subject to:

$$\begin{cases} \boldsymbol{\eta}(\bar{x}, x_1, x, t, t_1, \Delta\boldsymbol{v}_1) = 0 \\ \bar{\boldsymbol{r}} - \boldsymbol{r} = 0 \\ \bar{\boldsymbol{v}} - (\boldsymbol{v} + \Delta\boldsymbol{v}_2) = 0 \end{cases} \tag{26}$$

3.4. Necessary conditions

Starting from the definition of $\mathscr{J}$ given by equation (11) and taking into account equation (26), a well-defined constrained optimization problem is obtained with 11 scalar unknowns $[\bar{x}, x_1, x, t_1, t, \Delta\boldsymbol{v}_1, \Delta\boldsymbol{v}_2]$ and 9 constraints. The problem can be converted in an unconstrained optimization problem defining the augmented performance index $\mathscr{H}$, also known as the Hamiltonian, with the introduction of the Lagrange multipliers $\boldsymbol{\lambda}, \boldsymbol{\phi}, \boldsymbol{\psi} \in \mathscr{R}^3$ [10]:

$$\mathscr{H} = \mathscr{J}(\Delta\boldsymbol{v}_1, \Delta\boldsymbol{v}_2) + \boldsymbol{\lambda}^T\boldsymbol{\eta}(\bar{x}, x_1, x, t, t_1, \Delta\boldsymbol{v}_1) + \boldsymbol{\phi}^T(\bar{\boldsymbol{r}} - \boldsymbol{r}) + \boldsymbol{\psi}^T(\bar{\boldsymbol{v}} - (\boldsymbol{v} + \Delta\boldsymbol{v}_2)) \tag{27}$$

The necessary conditions to minimize $\mathscr{H}$ with respect to the augmented variables are given by equations (28)–(34):

$$\frac{\partial\mathscr{H}}{\partial\bar{x}} = \lambda_1\frac{\partial\eta_1}{\partial\bar{x}} + \boldsymbol{\phi}^T\frac{\partial\bar{\boldsymbol{r}}}{\partial\bar{x}} + \boldsymbol{\psi}^T\frac{\partial\bar{\boldsymbol{v}}}{\partial\bar{x}} = 0 \tag{28}$$

$$\frac{\partial\mathscr{H}}{\partial x_1} = \lambda_2\frac{\partial\eta_2}{\partial x_1} + \lambda_3\frac{\partial\eta_3}{\partial x_1} - \boldsymbol{\phi}^T\frac{\partial\boldsymbol{r}}{\partial x_1} - \boldsymbol{\psi}^T\frac{\partial\boldsymbol{v}}{\partial x_1} = 0 \tag{29}$$

$$\frac{\partial\mathscr{H}}{\partial x} = \lambda_3\frac{\partial\eta_3}{\partial x} - \boldsymbol{\phi}^T\frac{\partial\boldsymbol{r}}{\partial x} - \boldsymbol{\psi}^T\frac{\partial\boldsymbol{v}}{\partial x} = 0 \tag{30}$$

$$\frac{\partial\mathscr{H}}{\partial t} = -\sqrt{\mu}(\lambda_1 + \lambda_3) + \boldsymbol{\phi}^T\left(\frac{\partial\bar{\boldsymbol{r}}}{\partial t} - \frac{\partial\boldsymbol{r}}{\partial t}\right) = 0 \tag{31}$$

$$\frac{\partial\mathscr{H}}{\partial t_1} = -\sqrt{\mu}\lambda_2 + \lambda_3\frac{\partial\eta_3}{\partial t_1} - \boldsymbol{\phi}^T\frac{\partial\boldsymbol{r}}{\partial t_1} - \boldsymbol{\psi}^T\frac{\partial\boldsymbol{v}}{\partial t_1} = 0 \tag{32}$$

$$\frac{\partial\mathscr{H}}{\partial\Delta\boldsymbol{v}_1} = \frac{\partial\mathscr{J}}{\partial\Delta\boldsymbol{v}_1} + \lambda_3\frac{\partial\eta_3}{\partial\Delta\boldsymbol{v}_1} - \boldsymbol{\phi}^T\frac{\partial\boldsymbol{r}}{\partial\Delta\boldsymbol{v}_1} - \boldsymbol{\psi}^T\frac{\partial\boldsymbol{v}}{\partial\Delta\boldsymbol{v}_1} = 0 \tag{33}$$

$$\frac{\partial\mathscr{H}}{\partial\Delta\boldsymbol{v}_2} = \frac{\partial\mathscr{J}}{\partial\Delta\boldsymbol{v}_2} - \boldsymbol{\psi}^T\boldsymbol{I}_{3\times3} = 0 \tag{34}$$

Those expressions can be manipulated and combined together to obtain two meaningful scalar equations h_1, h_2 denoted as *rendezvous conditions* and equivalent to equations (28)–(34) [10]:

$$h_1 = (\Delta\boldsymbol{v}_1^T - \Delta\boldsymbol{v}_2^T\boldsymbol{L}_1)\boldsymbol{L}_0^{-1}\left[\left(\frac{\partial\bar{\boldsymbol{r}}}{\partial\bar{x}} - \frac{\partial\boldsymbol{r}}{\partial x}\right) + \frac{r}{\sqrt{\mu}}\left(\frac{\partial\bar{\boldsymbol{r}}}{\partial t} - \frac{\partial\boldsymbol{r}}{\partial t}\right)\right] + \Delta\boldsymbol{v}_2^T\left(\frac{\partial\bar{\boldsymbol{v}}}{\partial\bar{x}} - \frac{\partial\boldsymbol{v}}{\partial x}\right) = 0 \tag{35}$$

$$h_2 = (\Delta\boldsymbol{v}_1^T - \Delta\boldsymbol{v}_2^T\boldsymbol{L}_1)\boldsymbol{L}_0^{-1}\left[l_2\frac{\partial\boldsymbol{r}}{\partial x} - \left(\frac{\sqrt{\mu}}{r_1}\frac{\partial\boldsymbol{r}}{\partial x_1} + \frac{\partial\boldsymbol{r}}{\partial t_1}\right)\right] + \Delta\boldsymbol{v}_2^T\left[l_2\frac{\partial\boldsymbol{v}}{\partial x} - \left(\frac{\sqrt{\mu}}{r_1}\frac{\partial\boldsymbol{v}}{\partial x_1} + \frac{\partial\boldsymbol{v}}{\partial t_1}\right)\right] = 0 \tag{36}$$

Where $\boldsymbol{L}_0$, $\boldsymbol{L}_1$ and l_2 are defined as follows:

$$\boldsymbol{L}_0 = \frac{\partial\boldsymbol{r}}{\partial\Delta\boldsymbol{v}_1} - \frac{1}{r}\frac{\partial\boldsymbol{r}}{\partial x}\frac{\partial\eta_3}{\partial\Delta\boldsymbol{v}_1} \tag{37}$$

$$\boldsymbol{L}_1 = \frac{\partial\boldsymbol{v}}{\partial\Delta\boldsymbol{v}_1} - \frac{1}{r}\frac{\partial\boldsymbol{v}}{\partial x}\frac{\partial\eta_3}{\partial\Delta\boldsymbol{v}_1} \tag{38}$$

$$l_2 = \frac{1}{r}\left(\frac{\sqrt{\mu}}{r_1}\frac{\partial \eta_3}{\partial x_1} + \frac{\partial \eta_3}{\partial t_1}\right) \tag{39}$$

Combining expressions 26, 35 and 36 the whole set of equations that satisfies the optimality conditions, the equations of motion and the constraints on the final state vectors is obtained as:

$$\begin{cases} \boldsymbol{\eta}(\bar{x}, x_1, x, t, t_1, \Delta\boldsymbol{v}_1) = 0 \\ \bar{\boldsymbol{r}} - \boldsymbol{r} = 0 \\ \bar{\boldsymbol{v}} - (\boldsymbol{v} + \Delta\boldsymbol{v}_2) = 0 \\ h_1(\bar{x}, x, t, t_1, \Delta\boldsymbol{v}_1, \Delta\boldsymbol{v}_2) = 0 \\ h_2(x_1, x, t, t_1, \Delta\boldsymbol{v}_1, \Delta\boldsymbol{v}_2) = 0 \end{cases} \tag{40}$$

Which is a non-linear system that has to be solved numerically to determine $[\bar{x}, x_1, x, t, t_1, \Delta\boldsymbol{v}_1, \Delta\boldsymbol{v}_2]^T \in \mathscr{R}^{11}$ that corresponds to a minimum of $\mathscr{J}$.

Then, since the parameters a_1, r, $\boldsymbol{r}_1$, $\boldsymbol{v}_1$ that appears in 40 are *a priori* unknowns, the four equations (18), (19), (24) and (25) have to be adjoined to the system and the relations 20 to 23 taken into account to derive a final set of equations whose solution is computed from the only knowledge of $[\boldsymbol{r}_0, \boldsymbol{v}_0]$ and $[\bar{\boldsymbol{r}}_0, \bar{\boldsymbol{v}}_0]$ at time t_0.

The whole system can be conveniently expressed as:

$$F(\boldsymbol{X}) = 0 \tag{41}$$

Where $\boldsymbol{X} = [a_1, x_1, x, \bar{x}, r, t_1, t, \boldsymbol{r}_1, \boldsymbol{v}_1, \Delta\boldsymbol{v}_1, \Delta\boldsymbol{v}_2]^T \in \mathscr{R}^{19}$ and F is given by:

$$\begin{cases} \frac{(\boldsymbol{v}_1+\Delta\boldsymbol{v}_1)^T(\boldsymbol{v}_1+\Delta\boldsymbol{v}_1)}{2} - \frac{\mu}{r_1} + \frac{\mu}{2a_1} = 0 \\ a_1 + a_1\left[\frac{\boldsymbol{r}_1^T(\boldsymbol{v}_1+\Delta\boldsymbol{v}_1)}{\sqrt{\mu a_1}}\sin\frac{x}{\sqrt{a_1}} + \left(\frac{r_1}{a_1} - 1\right)\cos\frac{x}{\sqrt{a_1}}\right] - r = 0 \\ f_0\boldsymbol{r}_0 + g_0\boldsymbol{v}_0 - \boldsymbol{r}_1 = 0 \\ \dot{f}_0\boldsymbol{r}_0 + \dot{g}_0\boldsymbol{v}_0 - \boldsymbol{v}_1 = 0 \\ \boldsymbol{\eta}(\bar{x}, x_1, x, t, t_1, \Delta\boldsymbol{v}_1) = 0 \\ \bar{f}\,\bar{\boldsymbol{r}}_0 + \bar{g}\bar{\boldsymbol{v}}_0 - f_1\boldsymbol{r}_1 - g_1(\boldsymbol{v}_1 + \Delta\boldsymbol{v}_1) = 0 \\ \dot{\bar{f}}\,\bar{\boldsymbol{r}}_0 + \dot{\bar{g}}\bar{\boldsymbol{v}}_0 - \dot{f}_1\boldsymbol{r}_1 - \dot{g}_1(\boldsymbol{v}_1 + \Delta\boldsymbol{v}_1) - \Delta\boldsymbol{v}_2 = 0 \\ h_1(\bar{x}, x, t, t_1, \Delta\boldsymbol{v}_1, \Delta\boldsymbol{v}_2) = 0 \\ h_2(x_1, x, t, t_1, \Delta\boldsymbol{v}_1, \Delta\boldsymbol{v}_2) = 0 \end{cases} \tag{42}$$

4. Numerical example

Before being applied in the context of a future Mars Sample Return mission, the algorithm developed in chapter 3 is tested on a reference case proposed by Shirazi et al. [11]. Two non-coplanar, elliptical Earth orbits are selected and an optimal solution is sought for the most efficient rendezvous trajectory between the two spacecrafts. The chaser is initially located at the perigee of its orbit while the target initial conditions are chosen such that transfer time and burn locations coincide with the already published results. This adjustment is needed since the previous work considers only an optimal transfer between the two orbits without any requirement on the phasing between two spacecrafts.

The whole set of initial classical orbital elements is given in Table 1 with a semi-major axis, e eccentricity, Ω right ascension of the ascending node, i inclination, ω argument of periapsis and θ true anomaly.

The optimal rendezvous trajectory is determined solving equation (41) knowing the state vectors $[\bar{\boldsymbol{r}}_0, \bar{\boldsymbol{v}}_0]$ and $[\boldsymbol{r}_0, \boldsymbol{v}_0]$ computed from data in Table 1 as follows [12]:

Table 1
Classical orbital elements for the test case orbits.

S/C	a (km)	e $(-)$	Ω (°)	i (°)	ω (°)	θ_0 (°)
Target	32,600	0.5	270	50	265	173.6664
Chaser	11,300	0.2	275	40	280	0

$$\begin{aligned} \bar{\boldsymbol{r}}_0 &= [30632.3974 \quad -9551.6183 \quad 36506.2697]^T\ km \\ \bar{\boldsymbol{v}}_0 &= [0.3969 \quad 1.9478 \quad 0.4731]^T\ km/s \\ \boldsymbol{r}_0 &= [-6657.0680 \quad -2158.1938 \quad -5722.5209]^T\ km \\ \boldsymbol{v}_0 &= [1.5883 \quad -7.0519 \quad 0.8119]^T\ km/s \end{aligned} \tag{43}$$

MATLAB® R2019a is used to implement the proposed algorithms and obtain the corresponding results. All computations are performed on a Lenovo Y50-70 running Ubuntu 18.04 LTS with an Intel® Core™ i7-4720HQ CPU @ 2.60 GHz processor and 8 GB RAM.

Local optimization techniques are adopted to numerically solve equation (41) and thus different trajectories can be generated depending on the provided initial guess $\boldsymbol{X}_0$. Multiple sub-optimal transfers are obtained as solutions of the Lambert problem and the closest one to the global optima is selected as initial guess for the developed optimization algorithm. If $\boldsymbol{X}_0$ is in the basin of $\boldsymbol{X}_{opt}$ the convergence of the iterative routines is guaranteed and a solution is found without trouble.

The fixed-time transfer admits two different solutions, one corresponding to a change in true anomaly $\Delta\theta < 180°$ and the other with $\Delta\theta > 180°$, where $\Delta\theta = \theta - \theta_1$ is the difference in the chaser's true anomaly between the two impulsive burns $\Delta\boldsymbol{v}_1$, $\Delta\boldsymbol{v}_2$. Only the second solution is considered here since it corresponds to the results already available in the literature.

Equation (41) is then solved taking 14.6 s average CPU time leading to the following optimal solution $\boldsymbol{X}_{opt}$:

$$\begin{aligned} a_1 &= 21751.0401\ km \\ x_1 &= 62.7782 \\ x &= 608.8852 \\ \bar{x} &= 382.2524 \\ r &= 26930.8146\ km \\ t_1 &= 911.7310\ s \\ t &= 24993.6024\ s \\ \boldsymbol{r}_1 &= [-3901.5075 \quad -7678.1036 \quad -3882.8137]^T\ km \\ \boldsymbol{v}_1 &= [4.1862 \quad -4.6727 \quad 3.1576]^T\ km/s \\ \Delta\boldsymbol{v}_1 &= [0.5811 \quad -0.7221 \quad 0.6432]^T\ km/s \\ \Delta\boldsymbol{v}_2 &= [-0.2126 \quad 0.0621 \quad -0.9821]^T\ km/s \end{aligned} \tag{44}$$

From which the corresponding performance index $\mathscr{J}_{opt}$, total Δv, transfer trajectory's time of flight TOF and chaser's final state vector $[\boldsymbol{r}, \boldsymbol{v}]$ are retrieved:

$$\begin{aligned} \mathscr{J}_{opt} &= 1.1433 \\ \Delta v_{tot} &= 2.1350\ km/s \\ TOF &= t - t_1 = 24081.8713\ s \\ \boldsymbol{r} &= [4660.0549 \quad 25936.6561 \quad 5553.6371]^T\ km \\ \boldsymbol{v} &= [-2.6126 \quad -0.9242 \quad -3.1136]^T\ km/s \end{aligned} \tag{45}$$

These results are inline with the ones obtained by the previous authors thus validating the proposed algorithm and implementation.

Finally, the classical orbital elements for the rendezvous trajectory are computed from $[\boldsymbol{r}_1, \boldsymbol{v}_1]$ and $[\boldsymbol{r}, \boldsymbol{v}]$ given by 44, 45 obtaining the results in Table 2 [12]. Fig. 1 depicts both the optimal transfer trajectory and the two initial orbits in an inertial reference frame centered on planet Earth.

The optimal solution $\boldsymbol{X}_{opt}$ is then validated comparing the obtained value $\mathscr{J}_{opt}$ with the performance indexes corresponding to multiple solutions of the Lambert problem for different values of t_1, t centered in the optimal ones presented in 44. From Figs. 2 and 3 is possible to verify that $\mathscr{J}_{opt} = \min_{[t_1,t]}\mathscr{J}$ thus validating the proposed approach.

Finally, different contour lines for both h_1, h_2 are plotted in Fig. 4 to demonstrate that $\boldsymbol{X} = \boldsymbol{X}_{opt}$ only if $h_1 = h_2 = 0$, namely if the two

Table 2
Optimal transfer trajectory's classical orbital elements in the test case scenario.

a_1 (km)	e $(-)$	Ω (°)	i (°)	ω (°)	θ_1 (°)	θ (°)
21751.0401	0.5737	273.9006	40.8897	304.6363	17.0650	217.0013

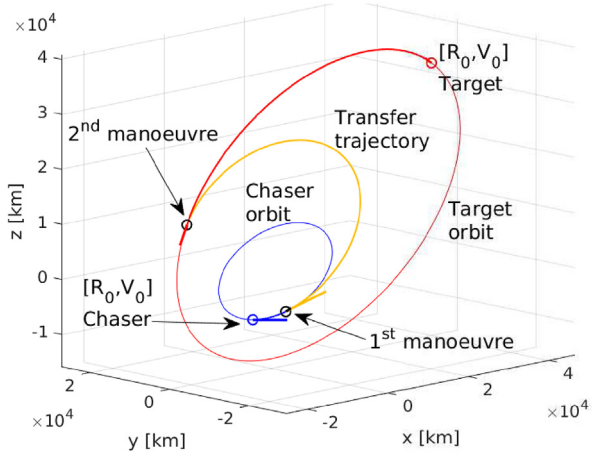

Fig. 1. Initial orbits and optimal transfer trajectory in the test case scenario.

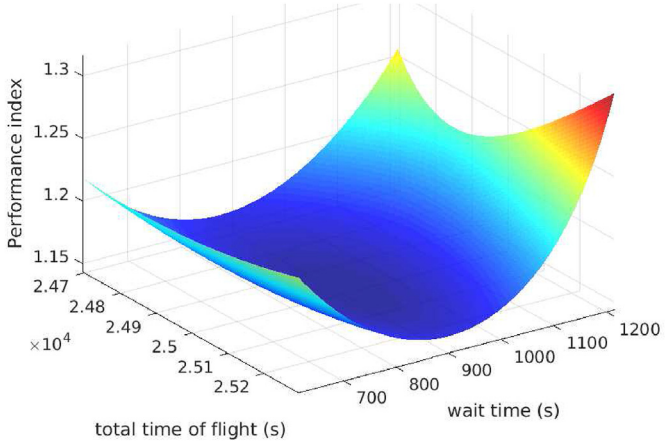

Fig. 2. Performance index $\mathscr{J}$ for varying t_1, t in the test case scenario.

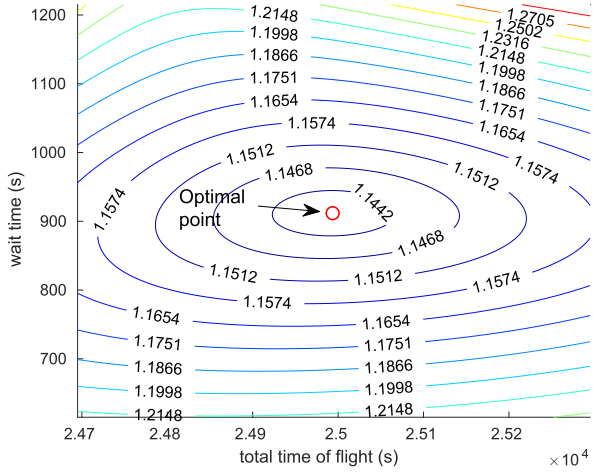

Fig. 3. Performance index $\mathscr{J}$ for varying t_1, t in the test case scenario.

rendezvous conditions are both satisfied.

5. Application to Mars Sample Return mission

5.1. Initial orbits

Due to the mission complexity and costs, the initial orbits of the two spacecrafts have to be chosen such that the probability of failure are minimized and an adequate scientific return is guaranteed. As a consequence, the landing mass of the probe that carries the OS down to the Mars surface has to be minimized to increase the chances of a successful touchdown. Since most of its weight is due to the propellant required to boost the OS back into orbit, the launch phase from the red planet has to be designed to minimize propellant consumption. On the other side, a minimum safe altitude must be achieved to ease the rendezvous manoeuvre performed by the SRO. For these reasons, a circular orbit at 500 km altitude with $i = 18.4386°N$ corresponding to a launch *due east* from Jezero Crater, the selected landing site for the Mars 2020 mission [15], has been chosen as a representative trajectory for the passive target.

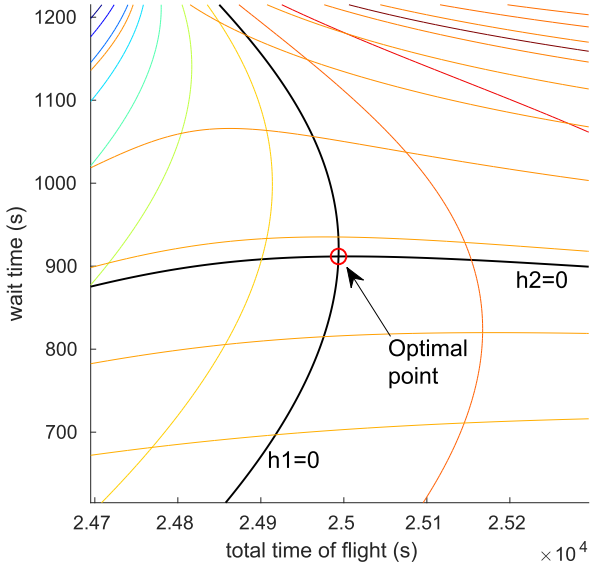

Fig. 4. Rendezvous conditions h_1, h_2 for varying t_1, t in the test case scenario.

On the other hand, the SRO will be equipped with appropriate scientific instruments to perform in-orbit measurements during surface operations of the lander. Due to its interesting properties, a sun-synchronous orbit with $a = 4222\ km$ and $e = 0.1362$ [16] has been finally selected as an ideal candidate for the SRO parking orbit.

The complete set of classical orbital elements that defines the spacecrafts initial orbits is presented in Table 3.

These data are then converted in the corresponding state vectors $[\bar{\boldsymbol{r}}_0, \bar{\boldsymbol{v}}_0]$ and $[\boldsymbol{r}_0, \boldsymbol{v}_0]$ to be employed in the solution of equation (41):

$$\begin{aligned}
\bar{\boldsymbol{r}}_0 &= [3897 \quad 0 \quad 0]^T\ km \\
\bar{\boldsymbol{v}}_0 &= [0 \quad 3.1449 \quad 1.0485]^T\ km/s \\
\boldsymbol{r}_0 &= [0 \quad -258.9441 \quad 3637.7956]^T\ km \\
\boldsymbol{v}_0 &= [-3.6528 \quad 0 \quad 0]^T\ km/s
\end{aligned} \tag{46}$$

As explained in section 4, depending on the provided initial guess two different solutions can be computed, one corresponding to a change in true anomaly $\Delta\theta < 180°$ and the other with $\Delta\theta > 180°$. Both of them have been considered in this study and the optimal rendezvous trajectories obtained from those guesses are presented in sections 5.2 and 5.4.

5.2. Short path scenario

A first optimal solution is searched between the transfer trajectories characterized by $\Delta\theta < 180°$. With an average CPU time lower than 3 s

Table 3
Classical orbital elements for the Mars Sample Return orbits.

S/C	$a\ (km)$	$e\ (-)$	$\Omega\ (°)$	$i\ (°)$	$\omega\ (°)$	$\theta_0\ (°)$
OS	3897	0	0	18.4386	0	0
SRO	4222	0.1362	0	94.0715	90	0

$\boldsymbol{X}_{opt}$ is then obtained as follows:

$$
\begin{aligned}
&a_1 = 4080.0510\ km\\
&x_1 = 508.5480\\
&x = 207.0184\\
&\bar{x} = 776.8537\\
&r = 3897\ km\\
&t_1 = 10194.4513\ s\\
&t = 14628.6477\ s\\
&\boldsymbol{r}_1 = [-4181.0932 \quad 32.6174 \quad -458.2276]^T\ km\\
&\boldsymbol{v}_1 = [-0.0867 \quad 0.2269 \quad -3.1876]^T\ km/s\\
&\Delta\boldsymbol{v}_1 = [-0.0982 \quad -2.0671 \quad 0.6486]^T\ km/s\\
&\Delta\boldsymbol{v}_2 = [0.5365 \quad 1.1153 \quad -1.6870]^T\ km/s
\end{aligned}
\tag{47}
$$

From which the corresponding performance index $\mathscr{J}_{opt}$, transfer trajectory's time of flight TOF and chaser's final state vector $[\boldsymbol{r}, \boldsymbol{v}]$ are retrieved:

$$
\begin{aligned}
&\mathscr{J}_{opt} = 4.5406\\
&TOF = t - t_1 = 4434.1964\ s\\
&\boldsymbol{r} = [3868.0498 \quad -449.7903 \quad -149.9619]^T\ km\\
&\boldsymbol{v} = [-0.1332 \quad 2.0062 \quad 2.7277]^T\ km/s
\end{aligned}
\tag{48}
$$

Finally, the classical orbital elements for the rendezvous trajectory are given in Table 4 while Fig. 5 depicts both the transfer trajectory and the two initial orbits in an inertial reference frame centered at planet Mars.

5.3. Validation of proposed numerical method for short path scenario

Similarly as before, the optimal solution $\boldsymbol{X}_{opt}$ is validated comparing the results with multiple solutions of the Lambert problem for different values of t_1, t. From Figs. 6 and 7 is possible to verify that $\mathscr{J}_{opt} = \min_{[t_1,t]}\mathscr{J}$ while Fig. 8 demonstrates that $\boldsymbol{X} = \boldsymbol{X}_{opt}$ only if $h_1 = h_2 = 0$, namely if the two rendezvous conditions are both satisfied.

5.4. Long path scenario

Following a similar approach, a second optimal solution is searched between the transfer trajectories with $\Delta\theta > 180°$. With an average CPU time of 5.3 s, the different components of $\boldsymbol{X}_{opt}$ are obtained as:

$$
\begin{aligned}
&a_1 = 4043.1058\ km\\
&x_1 = 718.0996\\
&x = 199.8981\\
&\bar{x} = 986.2006\\
&r = 3897\ km\\
&t_1 = 14830.2442\ s\\
&t = 18570.7816\ s\\
&\boldsymbol{r}_1 = [4176.0966 \quad 24.0371 \quad -337.6865]^T\ km\\
&\boldsymbol{v}_1 = [-0.1781 \quad -0.2275 \quad 3.1963]^T\ km/s\\
&\Delta\boldsymbol{v}_1 = [0.1636 \quad 2.0769 \quad -0.6604]^T\ km/s\\
&\Delta\boldsymbol{v}_2 = [0.2749 \quad -1.1442 \quad 1.6823]^T\ km/s
\end{aligned}
\tag{49}
$$

And the performance index $\mathscr{J}_{opt}$, transfer trajectory's time of flight TOF and chaser's final state vector $[\boldsymbol{r}, \boldsymbol{v}]$ are given by:

Table 4
Optimal transfer trajectory's classical orbital elements in the short path scenario.

$a_1\ (km)$	$e\ (-)$	$\Omega\ (°)$	$i\ (°)$	$\omega\ (°)$	$\theta_1\ (°)$	$\theta\ (°)$
4080.0510	0.1453	354.9746	53.9313	77.4148	110.3308	279.8565

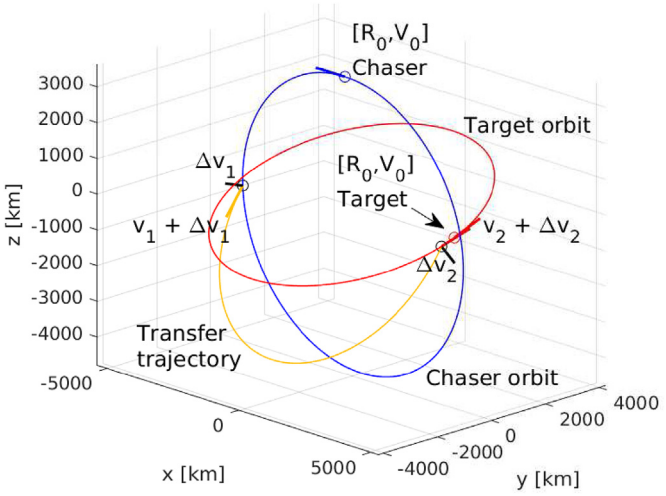

Fig. 5. Initial orbits and optimal transfer trajectory in the short path scenario.

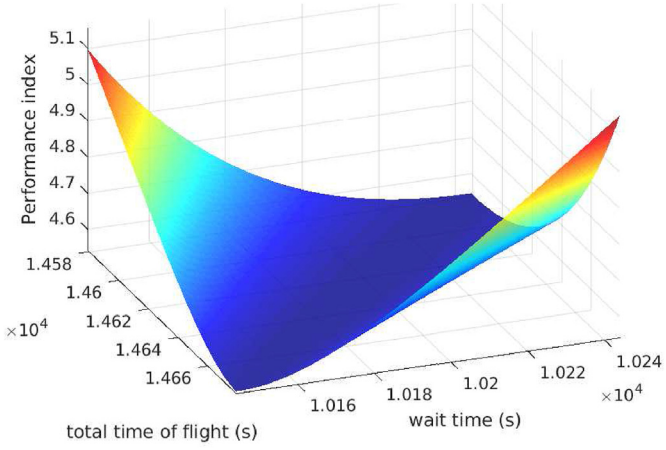

Fig. 6. Performance index $\mathscr{J}$ for varying t_1, t in the short path scenario.

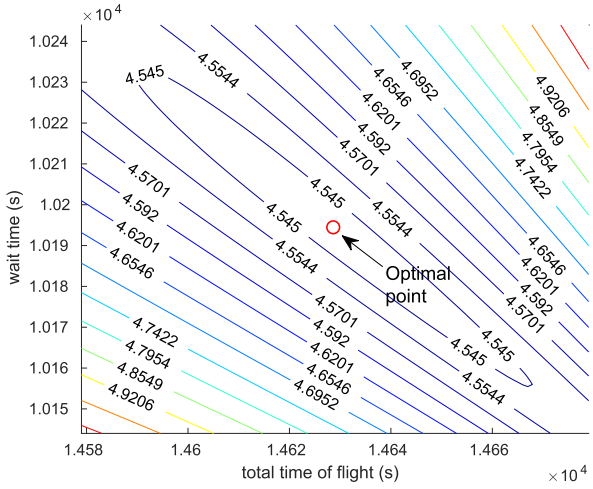

Fig. 7. Performance index $\mathscr{J}$ for varying t_1, t in the short path scenario.

$$
\begin{aligned}
&\mathscr{J}_{opt} = 4.4958\\
&TOF = t - t_1 = 3740.5374\ s\\
&\boldsymbol{r} = [-3881.2410 \quad -332.1370 \quad -110.7358]^T\ km\\
&\boldsymbol{v} = [0.0229 \quad -1.9880 \quad -2.7266]^T\ km/s
\end{aligned}
\tag{50}
$$

Finally, the classical orbital elements for the rendezvous trajectory

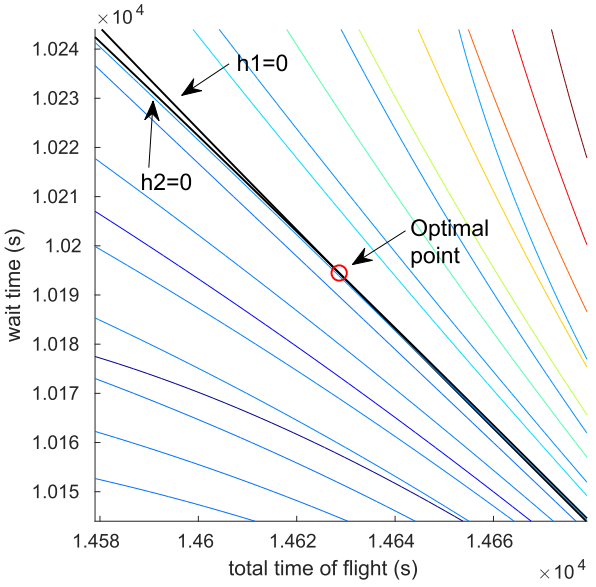

Fig. 8. Rendezvous conditions h_1, h_2 for varying t_1, t in the short path scenario.

Table 5
Optimal transfer trajectory's classical orbital elements in the long path scenario.

a_1 (km)	e $(-)$	Ω (°)	i (°)	ω (°)	θ_1 (°)	θ (°)
4043.1058	0.0756	3.7051	53.9405	116.7048	237.5733	65.3096

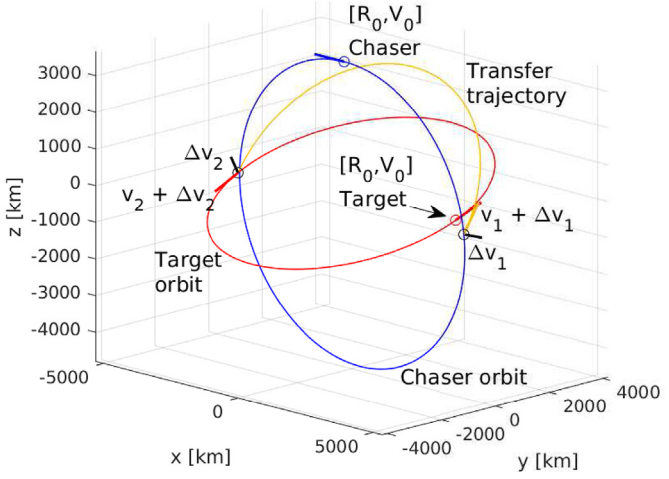

Fig. 9. Initial orbits and optimal transfer trajectory in the long path scenario.

are reported in Table 5. Fig. 9 depicts the different trajectories in the same reference frame as 5.

5.5. Validation of proposed numerical method for long path scenario

Once again, solving the Lambert problem for different values of t_1, t demonstrates that $\mathscr{J}_{opt} = \min_{[t_1,t]}\mathscr{J}$ as well as that $\boldsymbol{X} = \boldsymbol{X}_{opt}$ only if $h_1 = h_2 = 0$. Those results are illustrated in Figs. 10–12.

6. Effects of orbital perturbations

The extensive elaboration of data coming from the orbiting spacecrafts Mars Global Surveyor (MGS), Mars Odyssey and Mars Reconnaissance Orbiter (MRO) has produced in recent years noticeable improvement in the understanding of the characteristics of the Mars

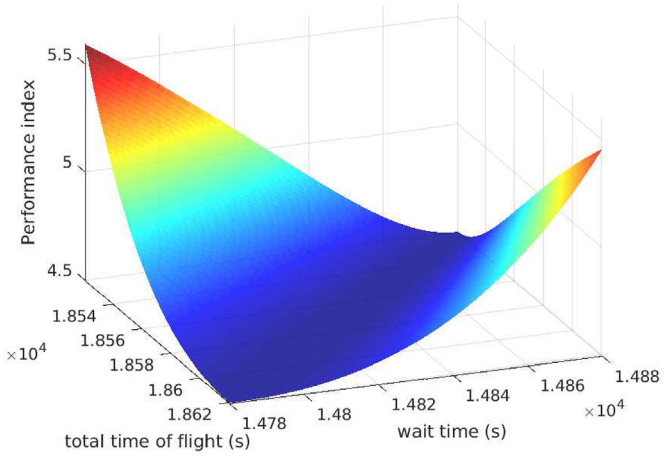

Fig. 10. Performance index $\mathscr{J}$ for varying t_1, t in the long path scenario.

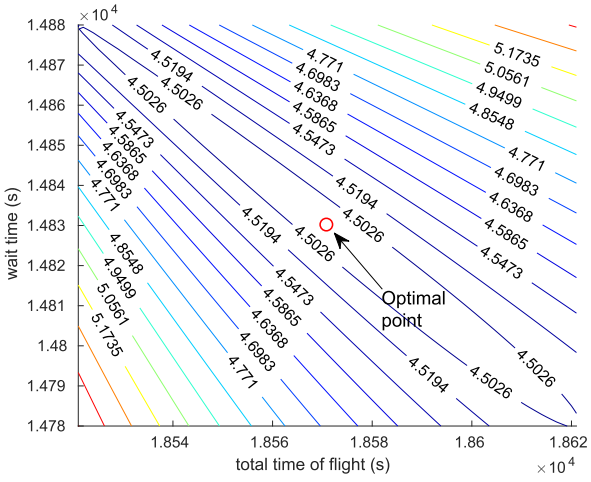

Fig. 11. Performance index $\mathscr{J}$ for varying t_1, t in the long path scenario.

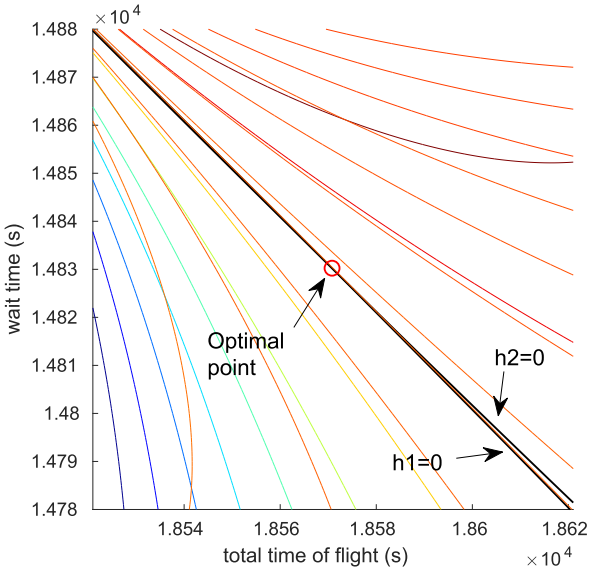

Fig. 12. Rendezvous conditions h_1, h_2 for varying t_1, t in the long path scenario.

gravitational field [17].

Orbital evolution of spacecrafts around the planet are in fact the results of a combined effect of Mars static gravitational field, time variation of the gravitational field induced by mass exchange between

the atmosphere and the ice caps (with periodicity linked to the 11 year cycle of solar activity) and time variation of the gravitational field induced by the tides. Contributions by non conservative forces as the ones by atmospheric drag and solar radiation pressure shall be taken into consideration depending on orbit type and altitude as well as third body effects due to Moons or the Sun.

When considering the baseline orbiting sample return mission in this work some contributions to Mars gravity field perturbation may be disregarded, due to their limited variation in the time range expected for the overall intercept manoeuvre (around 5 h) and just the effect of the Mars static field and solar radiation pressure may produce effective variations on orbital parameters.

Due to its lumpy character, the static gravitational field shall be simulated with a model with high order harmonics. While low order zonal harmonics are the most important factor affecting spacecraft's drift of motion, tesseral terms provide not negligible zero mean periodical oscillations. Although recently developed new JPL Mars gravity fields (MRO110B and MRO110B2) show resolution near degree 90, the model used in this work has been limited to order 60 by using a Goddard Mars Gravity Model 2 (GMM2).

The orbits of OS and SRO have been propagated using the GMM2 field model and considering solar radiation pressure for 365 days in order to investigate the worst case in terms of deviations of orbital parameters in a 5 h time range. Such maximum variations have been then considered as a 3 sigma 99.9% confidence uncertainty value to be taken into account for each Keplerian parameter in the optimization algorithm. The results for orbit inclination, eccentricity, semi-major axis, AOP and RAAN are reported in Figs. 13–15.

As a result, the 3 sigma uncertainty values reported in Table 6 have been considered for OS and SRO in a 5 and 4 h time range respectively.

At this point a systematic analysis has been conducted to determine the impact of those changes in the overall Δv required for the rendezvous manoeuvre. For both short and long path scenarios four different parametric studies have been performed applying those variations after the orbit propagation step carried out in the restricted two-body problem approximation with the Lagrange coefficients. The new required Δv has been then determined for a wide range of values bounded by the worst case scenarios presented in Table 6.

6.1. Variation of OS parameters in the short path scenario

Firstly, an analysis has been conducted considering nominal values for the SRO orbital parameters and evaluating the required energy to correctly perform the final rendezvous manoeuvre when the target spacecraft is no more in its nominal orbit. Two studies have been conducted varying first the OS semi-major axis and eccentricity and then its inclination and RAAN. The corresponding results are presented in Fig. 16.

From the same picture is possible to conclude that even if in most of the cases the presence of uncertainties leads to an increase in the overall Δv, in some circumstances those perturbations are beneficial thus resulting in a lower effort for the SRO. To summarize, a maximum increase of about 0.34 km/s has been observed due to a combined variation in the target's inclination and RAAN.

6.2. Variation of SRO parameters in the short path scenario

The second analysis has been carried out varying the SRO orbital parameters in the same manner described for the OS. The obtained results are presented in Fig. 17.

Similarly as before, the orbital perturbations are not always harmful but they may help the SRO while performing the rendezvous with the target OS. For this scenario the worst case variation results from an increase in the SRO inclination and requires and additional 0.12 km/s velocity change.

6.3. Variation of OS parameters in the long path scenario

Once the consequences of a more accurate gravity model and the solar radiation pressure were analyzed in the short path scenario, the same studies have been conducted for the longest solution and similar conclusions have been drawn. For a variation in the OS parameters graphical results are reported in Fig. 18.

In this case a maximum increase of 0.45 km/s is observed when the OS RAAN and inclination are both reduced by 1°.

6.4. Variation of SRO parameters in the long path scenario

Finally, differences in the SRO nominal parameters at the beginning of the first manoeuvre were added to the optimization framework and the corresponding deviations in the obtained results are depicted in Fig. 19.

The worst case is represented by a combined increase in both inclination and RAAN from their nominal values corresponding to an additional Δv of about 0.18 km/s.

To summarize, the orbital perturbations causes the OS and SRO orbits to slightly diverge from their nominal path, thus requiring additional correction manoeuvres to successfully accomplish the final rendezvous. As expected, the additional Δv due to deviations in inclination and RAAN is one order of magnitude higher than the one resulting from variations in semi-major axis and eccentricity, since the first requires an out-of-plane component of the manoeuvre to modify

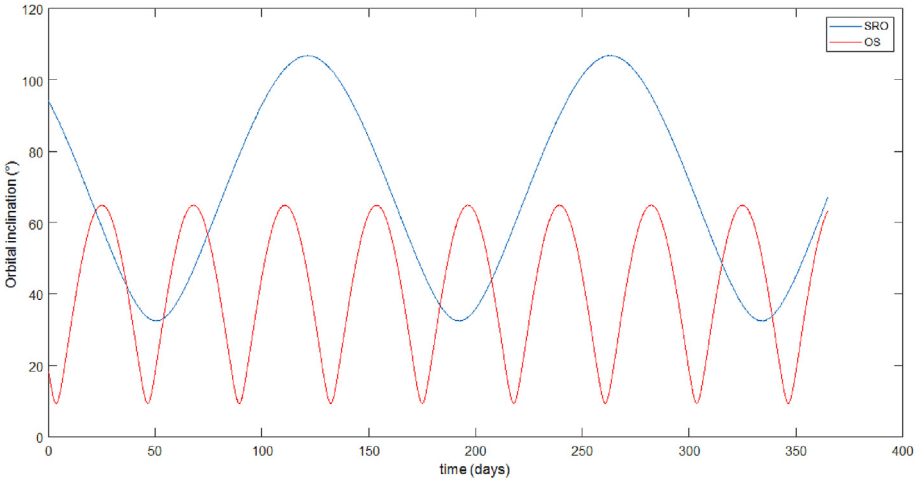

Fig. 13. Variation in inclination for OS and SRO.

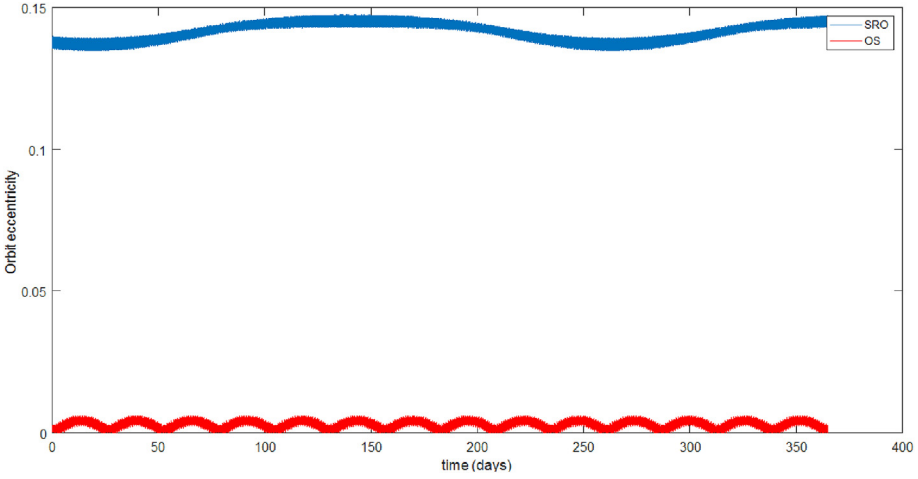

Fig. 14. Variation in eccentricity for OS and SRO.

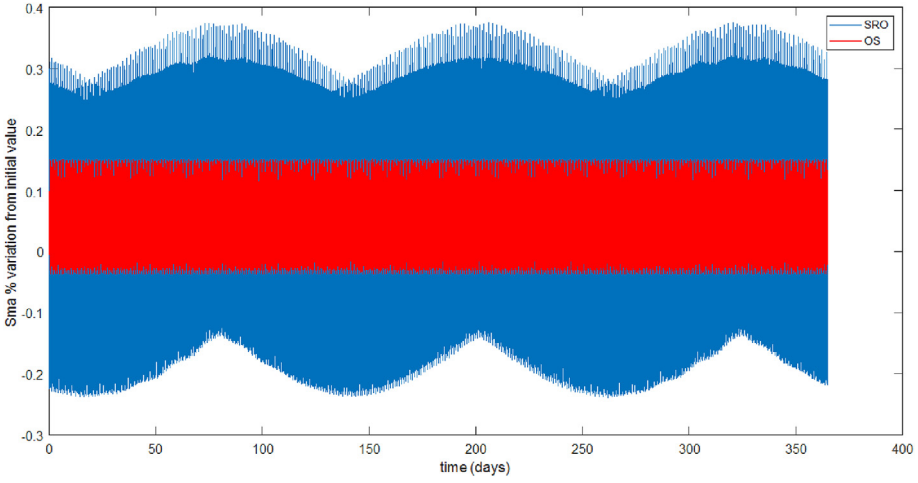

Fig. 15. Variation in semi-major axis for OS and SRO.

Table 6
Worst case variations of the OS and SRO orbital parameters.

S/C	$a\ (km)$	$e\ (-)$	$\Omega\ (°)$	$i\ (°)$	$\omega\ (°)$
OS	± 6.0	± 0.003	± 1.0	± 1.0	± 90.0
SRO	± 18.0	± 0.004	± 0.8	± 0.2	± 1.0

the direction of the SRO angular momentum vector.

Finally, a maximum increase in the required Δv of 0.45 km/s has been observed in the long path scenario when both inclination and RAAN of the OS are reduced by 1°. Even if not negligible, this value represents only less than 5% of the overall Δv required to perform the rendezvous in nominal conditions.

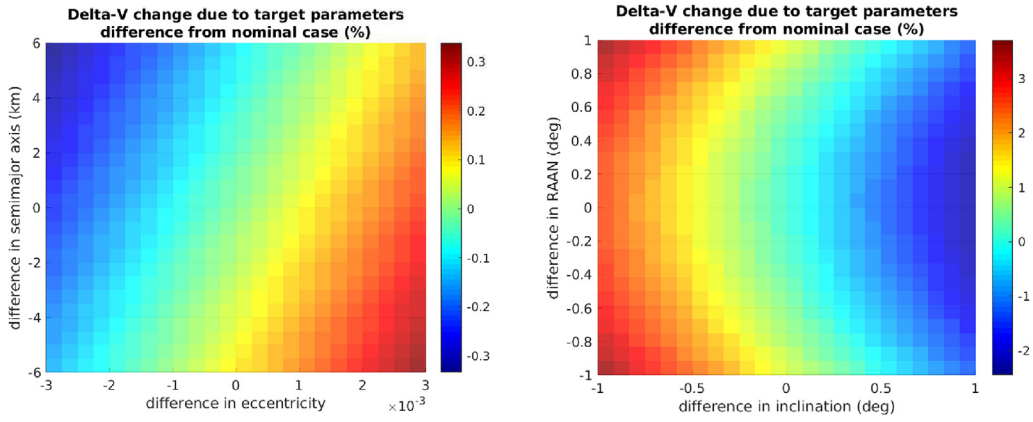

Fig. 16. Variation in Δv due to differences in OS orbital parameters in the short path scenario.

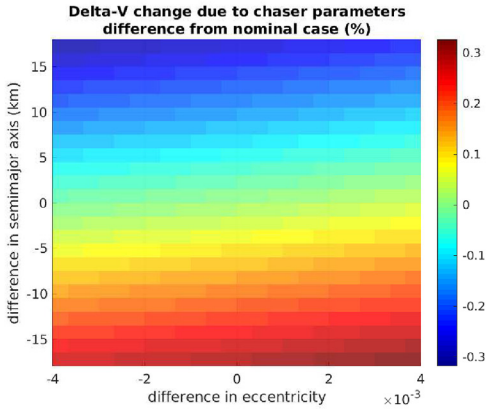

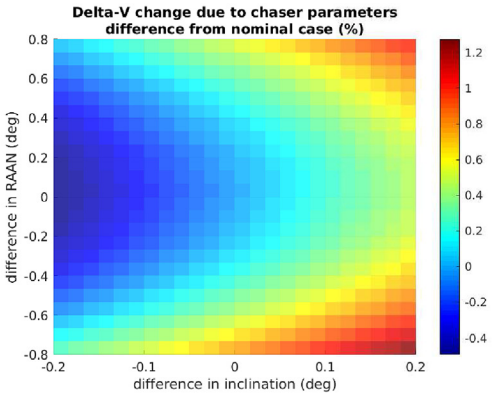

Fig. 17. Variation in Δv due to differences in SRO orbital parameters in the short path scenario.

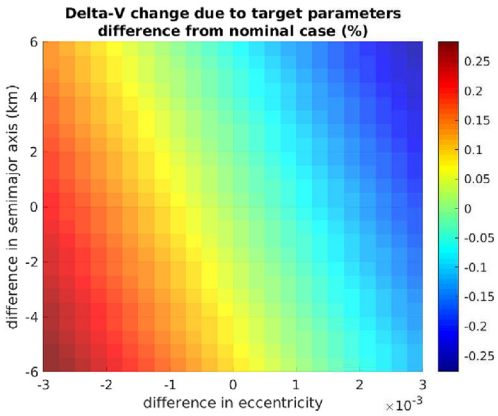

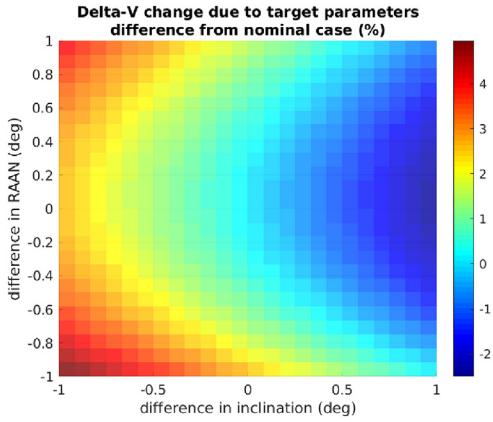

Fig. 18. Variation in Δv due to differences in OS orbital parameters in the long path scenario.

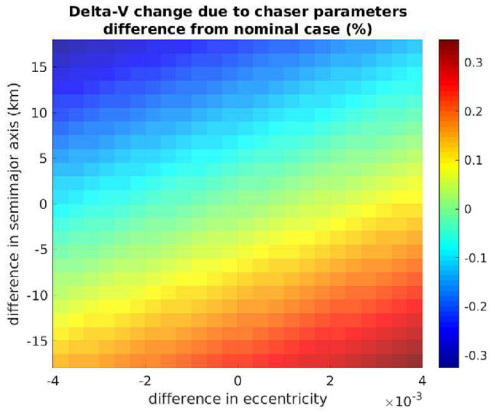

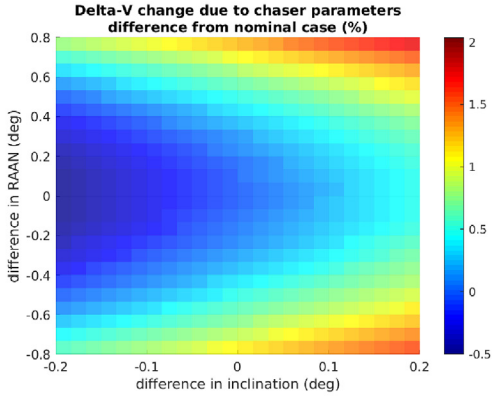

Fig. 19. Variation in Δv due to differences in SRO orbital parameters in the long path scenario.

7. Conclusions

The optimal control problem of finding the most fuel-efficient rendezvous trajectory between a chaser and a target satellite in non-coplanar orbits was analyzed considering wait time and total time of flight as free parameters to be determined through the solution of the problem itself. The two conditions to guarantee a minimum of the performance index were firstly revised and then adjoined with the required relations to obtain a system of equations whose solution is the optimal transfer trajectory. The proposed approach was then applied in the context of a Mars Sample Return mission to compute two possible rendezvous trajectories between SRO and OS. The obtained results were finally compared to the solution of the Lambert problem to demonstrate the effectiveness of the conducted work.

On the other hand, the proposed solution was obtained in the restricted two-body problem framework and only purely impulsive manoeuvres were admitted. An extensive study has been then conducted to estimate the impact of different orbital perturbations in the manoeuvre design. The Mars static gravitational field and the solar radiation pressure have been considered to determine the worst case variations in the SRO and OS orbital parameters in a time range comparable to the mission duration. When those perturbations are no more neglected an increase of about 5% in the manoeuvring Δv has to be considered for the worst case scenario. Even so, significant simplifications are still present in the proposed model and the algorithm is not applicable when a highly accurate solution is required. Suitable rendezvous strategies and automated guidance algorithms must be then considered to guarantee a safe manoeuvre and the spacecrafts integrity [18,19]. The aforementioned guidance laws are based on the study of the target and chaser relative dynamics and beyond the scope of the conducted work. However, given its low computational cost makes the proposed approach desirable for feasibility studies and trade-off

analysis in the context of a high-level mission design.

Declaration of competing interest

None.

Acknowledgements

This research did not receive any specific grant from funding agencies in the public, commercial, or not-for-profit sectors.

References

[1] I.S.E.C. Group, The Global Exploration Roadmap, Tech. rep, Aug. 2013.
[2] J.-M. Salotti, R. Heidmann, Roadmap to a human Mars mission, Acta Astronaut. 104 (2) (2014) 558–564, https://doi.org/10.1016/j.actaastro.2014.06.038 https://linkinghub.elsevier.com/retrieve/pii/S0094576514002379.
[3] G. Genta, J.-M. Salotti, A. Dupas, Global Human Mars System Missions Exploration, Goals, Requirements and Technologies, Cosmic Study of the International Academy of Astronautics, 2016.
[4] F. Alibay, Z.J. Bailey, Trade space evaluation of ascent and return architectures for a Mars Sample Return mission, 2014 IEEE Aerospace Conference, IEEE, Big Sky, MT, USA, 2014, pp. 1–16, , https://doi.org/10.1109/AERO.2014.6836323 http://ieeexplore.ieee.org/document/6836323/.
[5] R. Shotwell, J. Benito, A. Karp, J. Dankanich, A Mars Ascent Vehicle for potential mars sample return, 2017 IEEE Aerospace Conference, IEEE, Big Sky, MT, USA, 2017, pp. 1–12, , https://doi.org/10.1109/AERO.2017.7943851 http://ieeexplore.ieee.org/document/7943851/.
[6] D.J.P. MouraiMARS Team, The road to an international architecture for mars sample return: the IMARS team view, Proceedings of the International Astronautical Congress (IAC), 2008 IAC-08-A3.1.3.
[7] S. Perino, D. Cooper, D. Rosing, L. Giersch, Z. Ousnamer, V. Jamnejad, C. Spurgers, M. Redmond, M. Lobbia, T. Komarek, D. Spencer, The evolution of an orbiting sample container for potential Mars sample return, 2017 IEEE Aerospace Conference, IEEE, Big Sky, MT, USA, 2017, pp. 1–16, , https://doi.org/10.1109/AERO.2017.7943979 http://ieeexplore.ieee.org/document/7943979/.
[8] L.A. D'Amario, W.E. Bollman, W.J. Lee, R.B. Roncoli, J.C. Smith, Mars Orbit Rendezvous Strategy for the Mars 2003/2005 Sample Return Mission, Tech. rep., Jet Propulsion Laboratory, California Institute of Technology, Feb. 1999.
[9] H. Leeghim, Spacecraft intercept using minimum control energy and wait time, Celestial Mech. Dyn. Astron. 115 (1) (2013) 1–19, https://doi.org/10.1007/s10569-012-9448-5 http://link.springer.com/10.1007/s10569-012-9448-5.
[10] S. Oghim, S.-H. Mok, H. Leeghim, Optimal spacecraft rendezvous by minimum velocity change and wait time, Adv. Space Res. 60 (6) (2017) 1188–1200, https://doi.org/10.1016/j.asr.2017.06.025 https://linkinghub.elsevier.com/retrieve/pii/S0273117717304519.
[11] A. Shirazi, J. Ceberio, J.A. Lozano, An evolutionary discretized Lambert approach for optimal long-range rendezvous considering impulse limit, Aero. Sci. Technol. 94 (2019) 105400, https://doi.org/10.1016/j.ast.2019.105400 https://linkinghub.elsevier.com/retrieve/pii/S127096381931586X.
[12] H.D. Curtis, Orbital Mechanics for Engineering Students, third ed. Edition, Elsevier aerospace engineering series, Elsevier, BH, Butterworth-Heinemann is an imprint of Elsevier, Amsterdam ; Boston, 2014.
[13] R.R. Bate, D.D. Mueller, J.E. White, Fundamentals of Astrodynamics, Dover Publications, New York, 1971.
[14] H. Leeghim, B.A. Jaroux, Energy-optimal solution to the Lambert problem, J. Guid. Contr. Dynam. 33 (3) (2010) 1008–1010, https://doi.org/10.2514/1.46606 http://arc.aiaa.org/doi/10.2514/1.46606.
[15] G. Hautaluoma, NASA Announces Landing Site for Mars 2020 Rover, (Nov. 2018).
[16] R. Oberto, Mars sample return, a concept point design by Team-X (JPL's advanced project design team), Proceedings, IEEE Aerospace Conference, vol. 2, IEEE, Big Sky, MT, USA, 2002, , https://doi.org/10.1109/AERO.2002.1035567 2–559–2–573 http://ieeexplore.ieee.org/document/1035567/.
[17] A.S. Konopliv, S.W. Asmar, W.M. Folkner, O. Karatekin, D.C. Nunes, S.E. Smrekar, C.F. Yoder, M.T. Zuber, Mars high resolution gravity fields from MRO, Mars seasonal gravity, and other dynamical parameters, Icarus 211 (1) (2011) 401–428, https://doi.org/10.1016/j.icarus.2010.10.004 https://linkinghub.elsevier.com/retrieve/pii/S0019103510003830.
[18] Y.-Z. Luo, Z.-J. Sun, Safe rendezvous scenario design for geostationary satellites with collocation constraints, Astrodynamics 1 (1) (2017) 71–83, https://doi.org/10.1007/s42064-017-0006-5 http://link.springer.com/10.1007/s42064-017-0006-5.
[19] P. Wang, Y. Guo, B. Wie, Orbital rendezvous performance comparison of differential geometric and ZEM/ZEV feedback guidance algorithms, Astrodynamics 3 (1) (2019) 79–92, https://doi.org/10.1007/s42064-018-0037-6 http://link.springer.com/10.1007/s42064-018-0037-6.